Degree of linear polarization in spectral radiances from water-viewing infrared radiometers

Joseph A. Shaw

Infrared radiances from water become partially polarized at oblique viewing angles through both emission and reflection. I describe computer simulations that show how the state of polarization for water varies with environmental conditions over a wavelength range of 3–15 μm with 0.05-μm resolution. Polarization at wavelengths longer than approximately 4 μm generally is negative (*p*, or vertical) and increases with incidence angle up to approximately 75°, beyond which the horizontally polarized reflected atmospheric radiance begins to dominate the surface emission. The highest *p* polarization (~4–10%) is found in the atmospheric window regions of approximately 4–5 and 8–14 μm. In the 3–5-μm spectral band, especially between 3 and 4 μm, reflected atmospheric radiance usually is greater than surface emission, resulting in a net *s* polarization (horizontal). The results of these simulations agree well with broadband measurements of the degree of polarization for a water surface viewed at nadir angles of 0–75°.

OCIS codes: 010.4450, 010.7340, 260.5430, 260.3060, 280.0280, 300.6340.

1. Introduction

Polarization adds a dimension to passive infrared sensing that can yield information about a source or its environment beyond that conveyed by brightness and spectral content. As sophisticated infrared sensors have become more widely available, infrared polarization[1] has evolved from its largely astronomical roots into fields as diverse as environmental remote sensing,[2–7] military surveillance,[8–15] and machine vision.[16,17] For example, in both ocean remote sensing and military surveillance, Fourier-transform infrared spectrometers are being used increasingly as passive emission spectroradiometers, sometimes without sufficient consideration of the instrument polarization sensitivity or the scene polarization state.

With the exception of water, Earth's natural environment is largely unpolarized at thermal infrared wavelengths. Therefore radiometric sea-surface measurements at large incidence angles require a polarization-dependent surface emissivity, and polarization may still cause errors if the instrument polarization sensitivity is not considered fully.[7] Furthermore, the polarization signature of water may lead to identification of false targets when polarimetric infrared sensors are used to search for man-made objects in an otherwise unpolarized thermal background. In these and similar applications, there is a need for quantitative estimates of the polarization state of infrared radiances from water. In short, there are still not sufficient answers to the questions of how much infrared polarization should be expected for a water-viewing radiometer, how it varies with wavelength, and why.

Water surfaces and clouds were some of the first partially polarized infrared sources discussed in the literature.[2–5] Egan and his colleagues[4] investigated infrared polarization with a polarimeter and computer calculations similar to those presented here. They measured infrared polarization for water surfaces and provided excellent insight into how the emitted and reflected radiances combine to produce the net polarization. Sidran[5] calculated sea-surface reflectivity and emissivity for the wavelength range of $0.1–10^5$ μm and discussed the polarization state of water emission, but did not explore polarization for combined emitted and reflected radiances.

To improve image contrast between ships and the ocean background, Cooper *et al.*[10,11,13] and Walker *et al.*[12] measured polarized images in the 3–5- and 8–12-μm wavelength bands, finding predominantly *p* polarization for the sea surface (≲10% at 8–12 μm, less at 3–5 μm). Sun glitter reduced the amount of *p* polarization and, especially in the short-wave band, often produced *s* polarization.

The author is with the Environmental Technology Laboratory, National Oceanic and Atmospheric Administration, 325 Broadway, Boulder, Colorado 80303-3328. His e-mail address is jshaw@etl.noaa.gov.

Received 21 September 1998; revised manuscript received 2 March 1999.

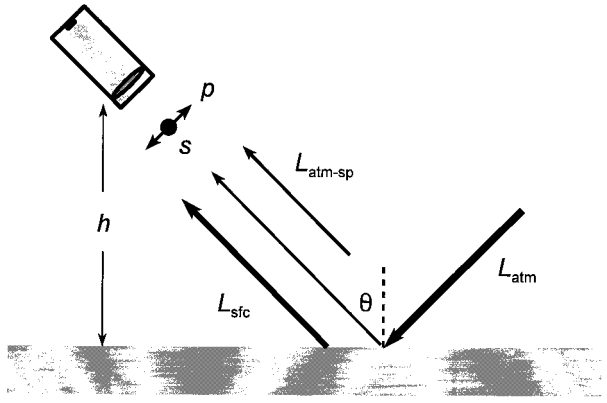

Fig. 1. Radiative transfer model simulates the radiance seen by a radiometer at height h viewing a water surface at nadir angle θ. The scene radiance comprises surface emission L_{sfc}, specular-angle atmospheric path emission L_{atm}, which is reflected at the surface, and short-path atmospheric path emission $L_{atm\text{-}sp}$. The total radiance is computed separately for s and p polarization (respectively, horizontal and vertical from the radiometer's viewpoint).

In this paper I answer the questions of how much polarization is expected for water-viewing radiometers under different environmental conditions and how the polarization varies with wavelength. Computer simulations allow the radiance components to be unraveled, thereby illuminating the physical principles that interact to create infrared polarization in the natural environment. Results are shown at 0.05-μm spectral resolution over the thermal infrared wavelength range of 3–15 μm, which covers the two important atmospheric transmission windows of approximately 3–5 and 8–14 μm. In Section 5 I show that the computed results agree well with measurements from a filter radiometer (9.9–11.5 μm).

2. Polarimetric Radiative Transfer Model

A. Overview

The computer model is written in the MATLAB language to compute polarization spectra for any given model of atmospheric emission, atmospheric transmission, and water refractive index. The atmospheric transmission and emission are calculated with the MODTRAN radiative transfer program,[18] and the water refractive index is from Hale and Querry.[19] Using another model for the infrared refractive index of water[20,21] or using the index for salt water[21] instead of pure water does not change these results in a fundamental way.

The model combines the radiative components illustrated in Fig. 1 to compute the total radiance seen by a sensor in two orthogonal linear polarization states. The water surface is assumed to be specular, with a rough surface modeled as a distribution of angled specular facets. The s- and p-polarization states are, respectively, perpendicular and parallel to the plane of incidence defined by the propagation vector of the detected radiance and the surface normal. From the radiometer's perspective, s is horizontal and p is vertical. Throughout this paper the two components of polarization-dependent quantities are denoted by superscripts s and p.

Referring to Fig. 1, a sensor at height h, viewing a water surface at nadir angle θ (the angle between the viewing direction and the nadir direction), sees a net radiance containing both surface and atmospheric terms. The radiance emitted by the surface is $L_{sfc}^{s,p}$, the radiance emitted by the atmospheric short path between the sensor and the surface is $L_{atm\text{-}sp}$ (independent of polarization), and the radiance emitted by the specular-angle atmospheric path is L_{atm} (all in units of W m^{-2} sr^{-1} μm^{-1}). The specular-path atmospheric radiance becomes partially polarized upon reflection from the surface according to the reflectivity $R_{sfc}^{s,p}$. Both the reflected atmospheric radiance and the surface-emitted radiance are attenuated by the short-path transmittance $\tau_{atm\text{-}sp}$. The combination of these elements, each of which is a function of angle θ and wavelength λ, produces the net radiance in each polarization state:

$$L^{s,p} = \tau_{atm\text{-}sp} L_{sfc}^{s,p} + L_{atm\text{-}sp} + \tau_{atm\text{-}sp} R_{sfc}^{s,p} L_{atm}. \quad (1)$$

For s- and p-polarized radiances L^s and L^p, respectively, the degree of polarization, DP, is

$$\mathrm{DP} = \frac{L^s - L^p}{L^s + L^p}. \quad (2)$$

The magnitude of the degree of polarization tells how polarized the light is and the sign tells its polarization direction (positive numbers indicate s polarization and negative numbers indicate p polarization).

B. Surface Radiance

The radiance emitted by the water surface at absolute temperature T is calculated as the product of a polarized emissivity $\epsilon_{sfc}^{s,p}$ and blackbody spectral radiance $L_{BB}(\lambda, T)$:

$$L_{sfc}^{s,p}(\lambda, \theta, T) = \epsilon_{sfc}^{s,p}(\lambda, \theta) L_{BB}(\lambda, T). \quad (3)$$

The blackbody spectral radiance L_{BB} is calculated from the Planck function:

$$L_{BB}(\lambda, T) = \frac{2 \times 10^{-6} hc^2}{\lambda^5} \left[\frac{1}{\exp\left(\frac{hc}{\lambda k T} \right) - 1} \right], \quad (4)$$

which contains Planck's constant h (6.6262×10^{-34} J s), the speed of light c (2.9979×10^8 m s^{-1}), and Boltzmann's constant k (1.3806×10^{-23} J K^{-1}). In Eq. (4) the wavelength has units of meters but the factor of 10^{-6} converts the result into units of W m^{-2} sr^{-1} μm^{-1}.

The polarization-dependent surface emissivity is equal to one minus the reflectivity:

$$\epsilon_{sfc}^{s,p}(\lambda, \theta) = 1 - R_{sfc}^{s,p}(\lambda, \theta). \quad (5)$$

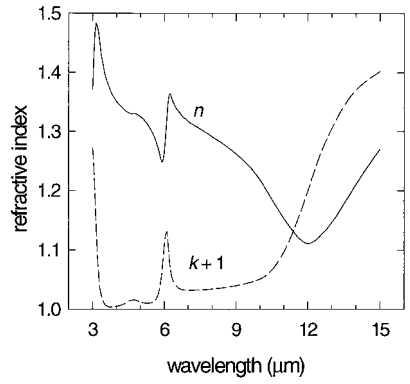

Fig. 2. Complex refractive index of water ($n - ik$).[19] The imaginary part is shown here as $k + 1$ for graphical convenience.

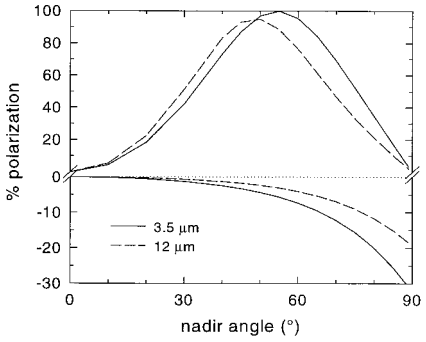

Fig. 4. Degree of polarization versus angle for water emission (bottom) and reflection (top) at the indicated wavelengths. Note the different vertical scales above and below 0%.

In Eq. (5), the s-polarized Fresnel reflectivity is[22]

$$R_{\mathrm{sfc}}{}^{s}(\lambda, \theta) = \left| \frac{\cos(\theta) - \tilde{n}(\lambda)\cos(\theta_r)}{\cos(\theta) + \tilde{n}(\lambda)\cos(\theta_r)} \right|^2, \tag{6a}$$

and the p-polarized Fresnel reflectivity is

$$R_{\mathrm{sfc}}{}^{p}(\lambda, \theta) = \left| \frac{\tilde{n}(\lambda)\cos(\theta) - \cos(\theta_r)}{\tilde{n}(\lambda)\cos(\theta) + \cos(\theta_r)} \right|^2, \tag{6b}$$

where $\tilde{n}(\lambda)$ is the complex refractive index of water, θ is the viewing angle with respect to nadir, and θ_r is the angle of refraction at the water–air interface:

$$\theta_r(\lambda, \theta) = \sin^{-1}\left[\frac{\sin(\theta)}{\tilde{n}(\lambda)} \right]. \tag{7}$$

The spectral variation of surface emission relative to a blackbody curve is determined by the refractive index of water, shown in Fig. 2;[19] the angular variation can be understood conceptually as emission just below the surface being refracted on transmission through the water–air interface.[1] Figure 3 shows the spectral emissivity of a smooth water surface viewed at 0° and 40°. The unequal polarization components at 40° illustrate how the surface emission becomes increasingly p polarized with increasing viewing angle. Up to the Brewster angle, the p component increases and the s component decreases relative to the nadir value. Beyond the Brewster angle both the p and s components fall below the nadir value, but always with the p component larger than the s component. Figure 3 also demonstrates the danger in assuming a constant emissivity as a function of either wavelength or angle.

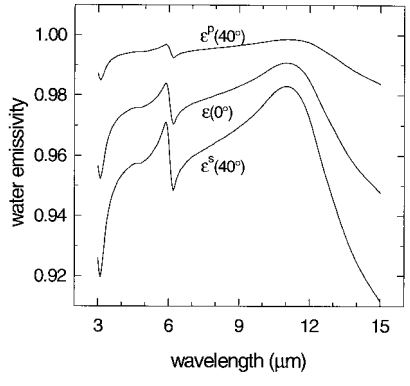

Fig. 3. Spectral emissivity of a smooth water surface viewed obliquely is partially polarized. As the angle increases, the p emissivity first rises and then falls below the nadir value while the s emissivity becomes steadily smaller.

A unique characteristic of emission polarization is that the degree of polarization magnitude increases monotonically with angle. The maximum surface-emission polarization occurs at 90° and is typically less than 30% for water in this spectral range. In contrast, reflection polarization increases with angle up to a maximum at the Brewster angle (typically ~48°–56° for water over this spectral range) and then decreases again to zero at 90°. The maximum value of reflection polarization at the Brewster angle is 100% for wavelengths that have negligible absorption and less elsewhere. These important characteristics of water emission and reflection polarization are illustrated in Fig. 4.

C. Atmospheric Radiance

The atmospheric radiance comprises emission from atmospheric gases in the short path between the sensor and the surface, as well as reflected emission from the specular-angle slant path. Also the short path (which is not so short for satellite or airborne instruments) between the instrument and the surface attenuates the surface-emitted and surface-reflected radiances. No polarization is included in either the short-path attenuation or emission. MODTRAN calculations of atmospheric emission and attenuation in this paper primarily use the 1976 U.S. Standard Atmosphere (USSA76), and the tropical and mid-latitude winter models where noted.[23]

Atmospheric-emitted radiance varies strongly with water-vapor content and cloud cover.[24,25] Figure 5 shows the calculated spectral atmospheric emission at the surface from a vertical atmospheric path that is clear and dry (black), clear and humid (blue), and dry but overcast with altostratus clouds (red). Understanding these curves is aided by recognizing that

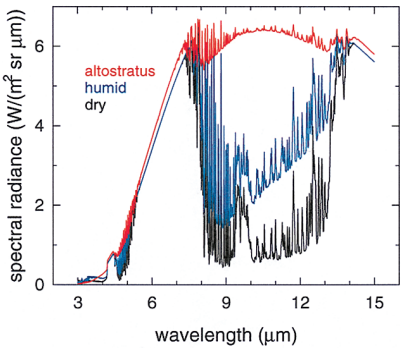

Fig. 5. Spectral atmospheric radiance (thermal emission and scattered solar) calculated for a vertical atmospheric path viewed from the surface. Both water vapor and clouds increase the radiance in the atmospheric transmission window regions of approximately 3–5 and 8–14 μm (the bottom two curves are for clear atmospheres that differ only in water-vapor content).

(1) atmospheric emissivity is equal to absorptivity in thermal equilibrium, so spectral regions of high emission relative to a blackbody curve also have low transmission; and (2) the radiance in highly absorbing regions approximates a blackbody curve at the local air temperature.

Clouds and water vapor both increase atmospheric absorption and emission and therefore increase the radiance emitted in the window regions of relatively high transmittance (e.g., 3–5 and 8–14 μm). In the extreme case of stratus clouds, the emission spectrum is similar to a blackbody at the cloud-base temperature. Although Fig. 5 shows atmospheric emission from a zenith path, other slant paths produce similar spectra, with the primary difference being that the longer atmospheric path lengths at larger zenith angles produce greater radiances in the window regions. The longer path length and higher surface reflectivity cause the total radiance at larger angles to contain an increasing amount of atmospheric radiance, which is *s* polarized because of the surface reflection.

Infrared atmospheric emission by itself is usually unpolarized. Although infrared atmospheric radiance can become partially polarized by aerosols, ice crystals, and water drops, the net degree of polarization rarely exceeds 5% for wavelengths longer than approximately 3.5 μm.[2,3,6] Multiple scattering and broad particle size distributions tend to obliterate most polarization signatures except in optically thin clouds such as thin cirrus. Such weakly polarized atmospheric radiance changes the results in Section 3 almost imperceptibly except at the shortest wavelengths, where the effect is no greater than that of reasonable changes to the aerosol model.

Scattered solar radiance usually is greater than thermal path radiance at wavelengths shorter than 4 μm but is negligible at longer wavelengths. The simulations shown here include scattered solar radiance, modeled using a maritime aerosol model[26] with 23-km visibility, a Henyey–Greenstein scattering phase function[26] with an asymmetry factor of zero, a 30° solar zenith angle, and a 0° solar azimuth angle. Other variations produce similar results, but the net polarization in the 3–4-μm spectral range could be affected strongly by the actual aerosol distribution.

3. Polarization of the Total Radiance

A. Effect of the Atmosphere

Unlike the numerically isolated elements in Section 2, any real measurement will consist of an inseparable mixture of emission and reflection polarization. Figure 6 shows the spectral degree of polarization calculated from the components described above for a smooth water surface viewed at 0°, 45°, 60°, and 75° from (a) 10-m altitude and (b) the top of the atmosphere (i.e., for a satellite-based radiometer). These

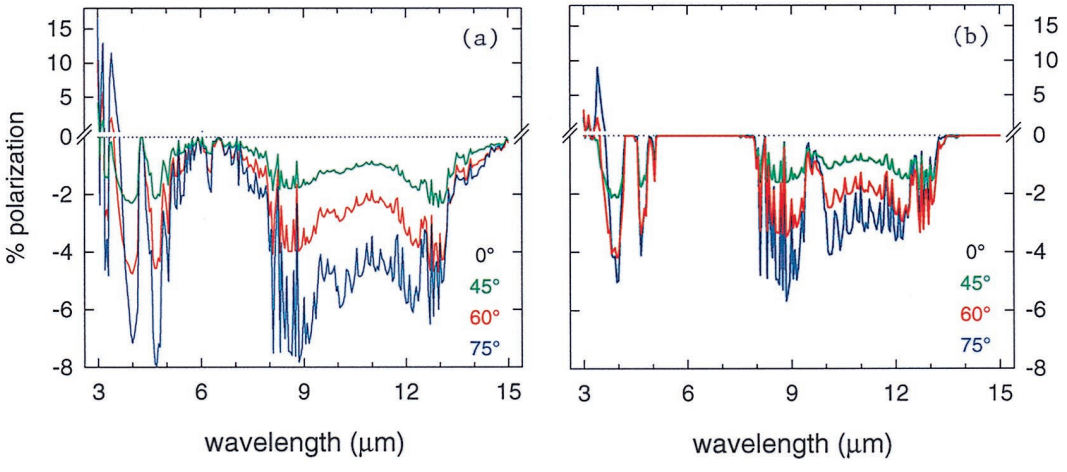

Fig. 6. Degree of polarization of the total radiance at different nadir angles for the USSA76 and sensors at (a) 10-m height and (b) top of atmosphere. A satellite-based sensor above the atmosphere sees a polarization signature that is similar to the near-surface value in the atmospheric transmission windows up to approximately 60°. Beyond this angle, the longer atmospheric path length for a satellite sensor greatly reduces the polarization from what is seen near the surface.

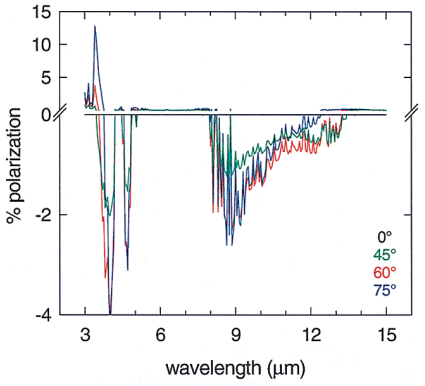

Fig. 7. Spectral degree of polarization of the total radiance for a smooth surface viewed from a 10-m height through a tropical atmosphere [compare with Fig. 6(a)]. The high water-vapor content greatly reduces the *p* polarization, especially in the 8–14-μm band, by absorbing surface-emitted radiance and by contributing to a greater reflected atmospheric radiance.

results are for a cloudless USSA76 model and a water temperature of 293 K.

The nadir views in Fig. 6 (dotted black lines) are unpolarized, but for other angles *p* polarization dominates at wavelengths longer than approximately 3.5 μm and *s* polarization dominates at shorter wavelengths. This is a result of the surface-emitted radiance being larger than the reflected atmospheric radiance at long wavelengths and vice versa at shorter wavelengths. High atmospheric attenuation prevents the surface from being seen well for wavelengths of approximately 5.5–7.5 μm, resulting in nearly zero polarization there. The most polarization occurs in the regions of highest atmospheric transmittance, primarily the 3–5- and 8–14-μm window bands.

A satellite-based radiometer [Fig. 6(b)] sees less polarization than one near the surface [Fig. 6(a)], largely because of the additional unpolarized atmospheric radiance between it and the water surface. For the example shown in Fig. 6(b), the polarization is zero for all angles at wavelengths between 5 and 8 μm and longer than 14 μm. Note also that the polarization is reduced less at angles below approximately 60° than at larger angles. It is at these large angles that the long optical paths between the surface and a satellite become most significant.

The polarization spectrum also changes significantly with the atmospheric state, even for a near-surface radiometer. Figure 7 shows the polarization spectrum for a near-surface radiometer (10-m height) viewing a water surface through a tropical atmosphere. The extremely high water-vapor content of the tropical atmosphere increases both the reflected atmospheric radiance and the short-path attenuation of the *p*-polarized surface-emitted radiance. As a result, for a tropical atmosphere, the polarization at 75° in the 8–14-μm band is actually less than at 60°. An additional interesting feature of this tropical case is that the *p* polarization is greater near 4 μm than anywhere in the 8–14-μm band.

The small-scale spectral features in the polarization spectra are also a result of the atmosphere. At wavelengths with high atmospheric absorption and emission, the surface-emitted radiance is reduced by absorption in the intervening atmosphere; furthermore, increased atmospheric emission at these wavelengths results in a larger reflected term, which reduces *p* polarization and enhances *s* polarization. Examples of these effects include the polarization nulls at the 4.3-μm and 14–15-μm CO_2 absorption bands and the 9.6-μm ozone band (the ozone band is clearly visible in Fig. 6, but emission from water vapor in the tropical atmosphere largely obliterates its signature in Fig. 7). Many other small-scale spectral features are also created by water-vapor absorption and emission.

Figure 8 shows the band-averaged degree of polarization as a function of nadir angle for several radi-

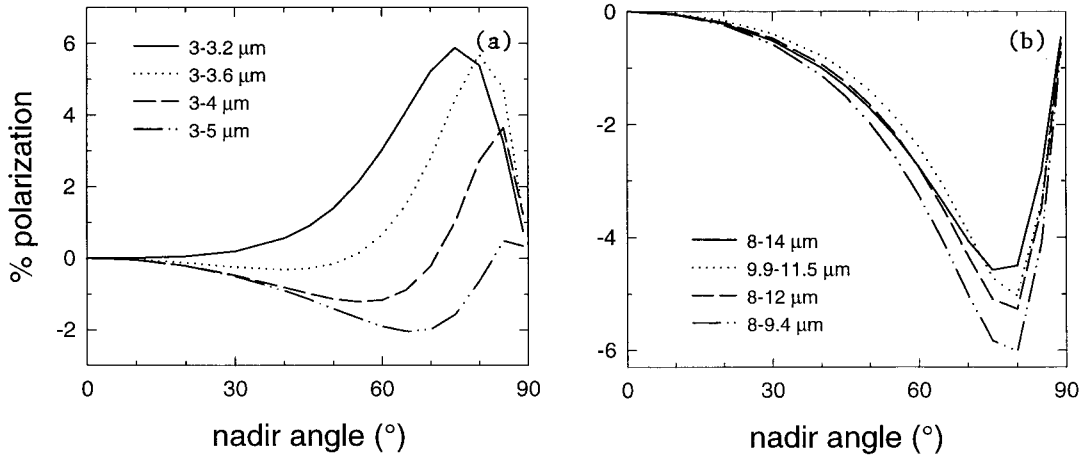

Fig. 8. Band-averaged degree of polarization for four (a) short-wave and (b) long-wave radiometer bands. The short-wave curves indicate dominant reflection polarization and the long-wave curves indicate dominant emission polarization. The magnitude of the long-wave polarization increases monotonically with angle up to approximately 75°, after which it decreases as the reflected atmospheric radiance begins to dominate the emitted surface radiance.

ometer bandwidths. The polarization behavior in the short-wave bands of Fig. 8(a) depends primarily on how far the bandwidth extends beyond 3.5 μm. Shorter wavelengths exhibit essentially pure *s* polarization, indicating that reflected sunlight exceeds thermal emission from the surface (note that in Subsection 3.C, even this shorter end of the spectrum is shown to exhibit *p* polarization at night). The short-wave bands that extend beyond 3.5 μm exhibit first *p* polarization, then *s* polarization as the angle is increased. Because of the significance of scattered sunlight, large changes in atmospheric water vapor, aerosols, or water temperature clearly can change the polarization signatures of these short-wave bands in a fundamental way.

The long-wave bands in Fig. 8(b) all behave similarly, with *p* polarization increasing until approximately 75° and then returning rapidly toward zero as the atmospheric radiance begins to dominate. Although Fig. 8 is for a USSA76, the drier mid-latitude winter atmosphere shifts the curves down, so that the polarization maxima are between −7% and −9%. Conversely, the humid tropical atmosphere model shifts the curves up, so that the maximum polarization is less than −2%.

Clouds have an effect rather similar to water vapor. The spectral degree of polarization is reduced by clouds because of the decreased radiometric contrast between a cloudy sky and a water surface. A water surface viewed under low stratus clouds appears to be unpolarized because the *s*-polarized sky reflection is nearly equal to the *p*-polarized surface emission. Thick cirrus and scattered high clouds have an effect similar to the higher-humidity tropical case shown in Fig. 7, whereas high, thin cirrus, especially in a fairly humid atmosphere, have little impact on the net polarization. In any case, clouds increase the reflected atmospheric radiance, thereby reducing the net *p* polarization, with the impact being largest for a dry and cool atmosphere.

B. Effect of Surface Roughness

Compared with a smooth surface, a wind-roughened water surface generally appears slightly less polarized below approximately 70° and more polarized at larger angles. As pointed out by Egan,[4] this reduction occurs because the projected area of wave facets with locally small incidence angles makes them more effective in determining the surface emissivity, resulting in an effectively smaller incidence angle. Surface roughness reduces the polarization at all angles in the monotonic emission polarization curves of Fig. 4. But it shifts the peak of the reflection polarization curves beyond the Brewster angle, causing the reflected polarization for a rough surface to be less than for a smooth surface below approximately 70° and greater at larger angles. The net effect of a rough surface is a combination of these two phenomena.

Figure 9 shows the spectral degree of polarization of a rough surface at 5-m s^{-1} wind speed for different nadir angles. Compared with the smooth-surface

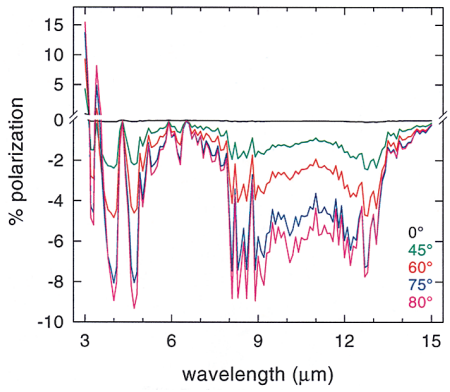

Fig. 9. Spectral degree of polarization of the total radiance for a rough surface (5-m s^{-1} wind speed) viewed at the indicated angles from a 10-m height through a USSA76 [compare with the corresponding smooth-surface curves in Fig. 6(a)]. The primary difference in the results with a rough surface is that the polarization magnitude continues to increase with angle up to at least 80°, whereas the smooth-surface polarization decreases beyond 75°.

results of Fig. 6(a), there is slightly less or equal polarization at each nadir angle up to approximately 75°. Figure 9 includes an additional curve at 80° to demonstrate that the polarization at such large angles is usually larger for a rough surface than for a smooth surface.

Surface roughness is modeled with an effective emissivity, calculated at each viewing angle by multiplying the Fresnel reflectivity and the slope probability density function and integrating over all slopes. The zero-order Gaussian term of the Cox–Munk slope probability model[27] was used in these calculations. Higher-order terms of the slope-probability density function yield a more accurate model of the surface,[27,28] but because their contribution to the slope integral is small, they are neglected here for simplicity. The detailed procedure for calculating the effective emissivity is described elsewhere.[29,30] However, Watts *et al.*[31] suggest that the actual effect of wind speed on surface emissivity is less than that predicted by this approach.

C. Effect of Sun and Moon Glints

Sun glints are specular reflections of sunlight from water. On a smooth water surface, only one glint appears at the solar specular angle. But on a wind-roughened water surface there are many glints, one for each wave facet whose orientation provides a specular solar reflection. Recall the commonly occurring glitter path or bright streak of dancing lights across a water surface at sunrise or sunset, which lengthens and broadens with surface roughness.[32] Sun glints are *s* polarized by reflection, so they reduce the net *p* polarization.

Infrared Sun glints are modeled by multiplying the radiance of a 5900 K blackbody by the atmospheric transmissivity and the surface reflectivity. Figure 10(a) shows the spectral degree of polarization at 60° for different values of glint area relative to the area seen by the radiometer (which makes the results in-

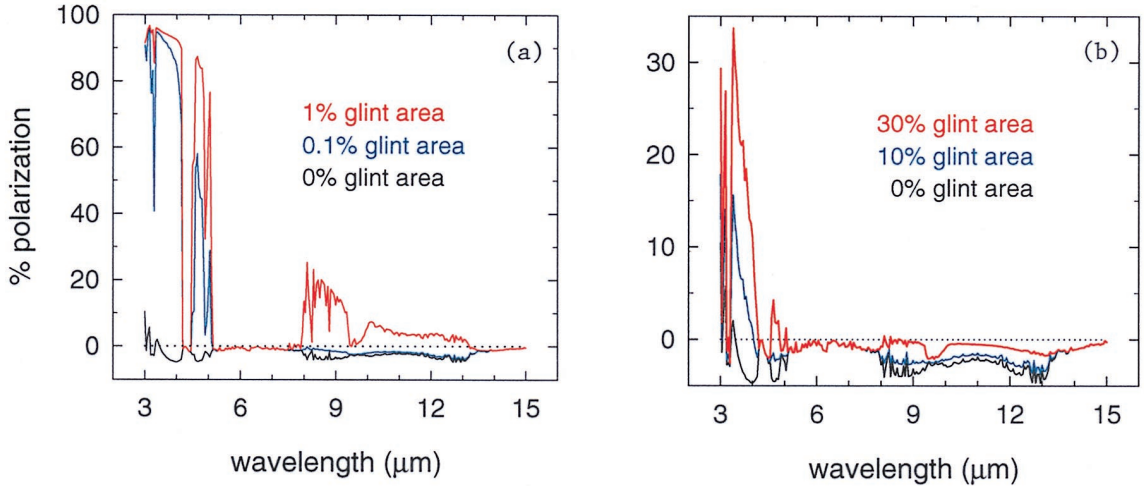

Fig. 10. Spectral degree of polarization for a water surface viewed at 60° with (a) Sun glints and (b) full-moon glints. Each curve is for a different percentage of the radiometer beam that contains glints.

dependent of sensor field of view). The scene becomes purely *s* polarized when as little as 1% of the total field of view contains Sun glints. These results agree qualitatively with previously reported measurements,[10] but should not be interpreted too strictly because they are valid only for specular, plane-surface facets. The curvature of individual wave facets on a wind-roughened surface could reduce the glint irradiance at the sensor, resulting in a smaller effect by glints on the net polarization.

The question of how infrared polarization changes at night is inevitable and interesting. Scattered lunar radiance is usually several orders of magnitude below the atmospheric thermal radiance, so the infrared nighttime atmosphere can be modeled with only the thermal-emission portion of the daytime calculation. Lunar radiance is a significant factor only with direct moon glints, which are considered here for the brightest case of a full moon.

Modeling the infrared moon requires both solar-reflection and thermal-emission terms (the lunar model in MODTRAN3 contains only solar reflection). The moon is a modestly strong reflector in the short-wave infrared and an efficient thermal emitter in the long-wave infrared. The reflectivity of the moon increases with wavelength throughout the short-wave infrared, to a value near 0.35 at approximately 4 μm, and then decreases to a relatively constant value in the range of 0–0.1 over the 8–14-μm wavelength range.[33,34] Multiplying this reflectivity by the radiance from a 5900 K blackbody is a simple, but adequate, model for the solar-reflection component of lunar radiance. Thermal emission from the full moon is modeled by multiplying the lunar emissivity (one minus reflectivity) by blackbody radiance at T = 390 K. A more complete model will require considering the variation of the moon's brightness with the lunar phase.[35]

Figure 10(b) shows the effect of moon glints on the net spectral polarization at 60° for several values of relative glint area, as in Fig. 10(a). Note first that the 0% glint-area curve shows significantly more short-wave *p* polarization without the scattered solar radiance compared with the daytime 0% Sun glint curve. As the relative glint area increases, the 3–5-μm region rapidly becomes strongly *s* polarized. The 8–14-μm polarization is altered more slowly, requiring more than 30% relative glint area before becoming *s* polarized.

4. Comparison of Measured and Calculated Long-Wave Polarization

Figure 11 shows a comparison of calculated and measured polarization. The measurements are from a filter radiometer with a 9.9–11.5-μm half-power bandwidth, a bolometer detector, a 4° field of view, and a rotating wire grid polarizer with an extinction ratio of approximately 200:1. The radiometer was mounted on a tripod and measured the polarized radiance from water in a plastic tub. The instrument offset was removed from each radiance value before computing the degree of polarization. Measurement

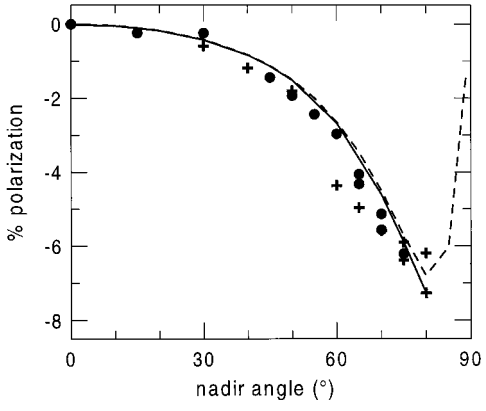

Fig. 11. Two sets of measured polarization (circles and crosses) compared with calculations for a smooth surface (dashed curve) and a rough surface at 1-m s^{-1} wind speed (solid curve), both using the mid-latitude winter atmosphere model.

uncertainty is estimated to be within 0.4% polarization (roughly twice the size of the symbols in Fig. 11) and within the symbol size for nadir angle.

The circles and crosses in Fig. 11 show the degree of polarization from two sets of measurements made outside under a clear, dry atmosphere (polarization was not detectable in the laboratory because of the low radiometric contrast between the water and the background). Each symbol represents an independent 1-s radiometer reading. The two sets of measurements were made within a 30-min period, during which no significant changes occurred in the atmosphere or water. The circles are the second measurement sequence, during which additional care was taken in measuring angles above 60° and avoiding partial clipping of the elongated radiometer beam at those angles. During the measurements, the air and water temperatures were 14.2 °C and 16.4 °C, respectively; the radiometer axis pointed west, with the Sun to the east southeast but blocked by a building, and the atmospheric path reflected by the water was clear to just past 75°). The air was calm, with light, intermittent breezes.

The dashed curve is the degree of polarization calculated for a smooth surface and the solid curve is the degree of polarization calculated for a rough surface with 1-m s^{-1} wind speed. The mid-latitude winter model atmosphere was used, even though its near-surface air temperature is too cool, because it provides a close match to the dry water-vapor profile on that day. The good agreement between the calculation results and the measurements is encouraging but also suggests the potential importance of surface roughness. However, better measurements above 75° and more-accurate atmospheric modeling will be required to test the important differences between the smooth and rough-surface calculations.

5. Discussion and Conclusions

Water surfaces have been shown through both calculation and measurement to be partially polarized at thermal infrared wavelengths. The significance of this polarization depends on (1) whether polarization is intended to be measured and (2) how sensitive the radiometer is to the polarization state of incident radiance. The polarization signatures discussed here certainly can be measured with minimal care if the polarization itself is of interest. However, for a sensor with minimal polarization sensitivity, these polarization signatures may not constitute a significant problem for radiometric measurements that are intended to be unpolarized. This is, nevertheless, a situation that is better determined carefully than assumed.

The degree of polarization for infrared radiances from water is maximized by a large radiometric contrast between the water and the atmosphere (or other background). The scene radiance is predominantly *p* polarized at wavelengths longer than approximately 3.5 μm, but *s*-polarized reflected atmospheric radiance decreases the *p* polarization when the atmosphere becomes brighter (e.g., by increased water vapor or clouds). Sun glints and full-moon glints add *s* polarization throughout the spectrum, but most notably at short wavelengths where solar radiation exceeds terrestrial thermal emission. Wind-generated surface roughness generally reduces polarization for nadir angles less than approximately 70° but increases it at larger angles. The degree of polarization measured with a long-wave radiometer agrees well with these calculations, but more measurements with a larger variety of conditions and wavelengths will be required to completely validate the model results.

I appreciate the contributions made by Heather Zorn (NOAA Environmental Technology Laboratory) in assisting with the polarization measurements, James H. Churnside (NOAA Environmental Technology Laboratory) for helpful discussions and encouragement, David Ansley of Raytheon for pointing out an important inconsistency in a preliminary manuscript, and the anonymous reviewers for their interest and useful suggestions. This document has been generated as part of a joint NOAA and U.S. Department of Defense Advanced Sensors Applications Program.

References

1. O. Sandus, "A review of emission polarization," Appl. Opt. **4,** 1634–1642 (1965).
2. F. F. Hall, Jr., "The effect of cirrus clouds on 8–13 μm infrared sky radiance," Appl. Opt. **7,** 891–898 (1968).
3. F. F. Hall, Jr., "A physical model of cirrus 8–13 μm infrared radiance," Appl. Opt. **7,** 2264–2269 (1968).
4. W. G. Egan, *Photometry and Polarization in Remote Sensing* (Elsevier, New York, 1985), pp. 337–354.
5. M. Sidran, "Broadband reflectance and emissivity of specular and rough water surfaces," Appl. Opt. **20,** 3176–3183 (1981).
6. Y. Takano and K. N. Liou, "Infrared polarization signature from cirrus clouds," Appl. Opt. **31,** 1916–1919 (1992).
7. J. A. Shaw, "The impact of polarization on infrared sea-surface temperature sensing," in *IGARSS '98* (Institute of Electrical and Electronics Engineers, New York, 1998), pp. 496–498.
8. R. D. Tooley, "Man-made target detection using infrared polarization," in *Polarization Considerations for Optical Systems II*, R. A. Chipman, ed., Proc. SPIE **1166,** 52–58 (1989).
9. T. J. Rogne, F. G. Smith, and J. E. Rice, "Passive target detection using polarized components of infrared signatures," in *Polarimetry: Radar, Infrared, Visible, Ultraviolet, and X-Ray*, R. A. Chipman and J. W. Morris, eds., SPIE Proc. **1317,** 242–251 (1990).
10. A. W. Cooper, E. C. Crittenden, Jr., E. A. Milne, P. L. Walker, E. Moss, and D. Gregoris, "Mid and far infrared measurements of sun glint from the sea surface," in *Optics of the Air-Sea Interface*, L. Estep, ed., Proc. SPIE **1749,** 176–185 (1992).
11. A. W. Cooper, W. J. Lentz, P. L. Walker, and P. M. Chan, "Infrared polarization measurements of ship signatures and background contrast," in *Characterization and Propagation of Sources and Backgrounds*, W. R. Watkins, ed., Proc. SPIE **2223,** 300–309 (1994).
12. P. L. Walker, W. J. Lentz, and A. W. Cooper, "Atmospheric and sea state dependence of polarized infrared contrast," in *Targets and Backgrounds: Characterization and Representation*, W. R. Watkins, ed., Proc. SPIE **2469,** 393–403 (1995).
13. A. W. Cooper, W. J. Lentz, and P. L. Walker, "Infrared polarization ship images and contrast in the MAPTIP experiment,"

in *Image Propagation through the Atmosphere*, J. Daintyll and R. Bissonnette, eds., Proc. SPIE **2828,** 85–96 (1996).
14. C. S. L. Chun, F. A. Sadjadi, and D. Ferris, "Automatic target recognition using polarization-sensitive, thermal imaging," in *Automatic Object Recognition V*, F. A. Sadjadi, ed., Proc. SPIE **2485,** 353–364 (1995).
15. D. L. Jordan, G. D. Lewis, and E. Jakeman, "Emission polarization of roughened glass and aluminum surfaces," Appl. Opt. **35,** 3583–3590 (1996).
16. M. Partridge and R. C. Saull, "Three-dimensional surface reconstruction using emission polarization," in *Image and Signal Processing for Remote Sensing II*, J. Desachy, ed., Proc. SPIE **2579,** 92–103 (1995).
17. F. Sadjadi and C. Chun, "Machine recognition of objects using IR polarimetry," *Automatic Object Recognition VI*, F. A. Sadjadi, ed., Proc. SPIE **2756,** 53–59 (1996).
18. A. Berk, L. S. Bernstein, and D. C. Robertson, "MODTRAN: a moderate resolution model for LOWTRAN7," AFGL Technical Report GL-TR-89-0122 (U.S. Air Force Geophysics Laboratory, Hanscom Air Force Base, Mass., 1989).
19. G. M. Hale and M. R. Querry, "Optical constants of water in the 200-nm to 200-μm wavelength region," Appl. Opt. **12,** 555–563 (1973).
20. W. M. Irvine and J. B. Pollack, "Infrared optical properties of water and ice spheres," Icarus **8,** 324–360 (1968).
21. D. Friedman, "Infrared characteristics of ocean water (1.5–15 μm)," Appl. Opt. **8,** 2073–2078 (1969).
22. M. Born and E. Wolf, *Principles of Optics*, 6th ed. (Pergamon, New York, 1991), p. 40.
23. G. P. Anderson, S. A. Clough, F. X. Kneizys, J. H. Chetwynd, and E. P. Shettle, "AFGL atmospheric constituent profiles (0–120 km)," AFGL Technical Report AFGL-TR-86-0110 (U.S. Air Force Geophysics Laboratory, Hanscom Air Force Base, Mass., 1986).
24. Y. Han, J. A. Shaw, J. H. Churnside, P. D. Brown, and S. A. Clough, "Infrared spectral radiance measurements in the tropical Pacific atmosphere," J. Geophys. Res. **102,** 4353–4356 (1997).
25. J. A. Shaw, J. B. Snider, J. H. Churnside, and M. D. Jacobson, "Comparison of infrared atmospheric brightness temperatures measured by a Fourier transform spectrometer and filter radiometer," J. Atmos. Oceanic Technol. **12,** 1124–1128 (1995).
26. E. P. Shettle, "Models of aerosols, clouds and precipitation for atmospheric propagation studies," in *Atmospheric Propagation in the UV, Visible, IR and mm-Wave Region and Related Systems Aspects* (Advisory Group for Aerospace Research and Development, Paris, 1989), pp. 15-3–15-13.
27. C. Cox and W. Munk, "Measurement of the roughness of the sea surface from photographs of the sun's glitter," J. Opt. Soc. Am. **44,** 838–850 (1954).
28. J. A. Shaw and J. H. Churnside, "Scanning-laser glint measurements of sea-surface slope statistics," Appl. Opt. **36,** 4202–4213 (1997).
29. X. Wu and W. L. Smith, "Emissivity of rough sea surface for 8–13 μm: modeling and verification," Appl. Opt. **36,** 2609–2619 (1997).
30. K. Masuda, T. Takashima, and Y. Takayama, "Emissivity of pure and sea waters for the model sea surface in the infrared window regions," Remote Sens. Environ. **24,** 313–329 (1988).
31. P. D. Watts, M. R. Allen, and T. J. Nightingale, "Wind speed effects on sea surface emission and reflection for the Along Track Scanning Radiometer," J. Atmos. Oceanic Technol. **13,** 126–141 (1996).
32. J. A. Shaw, "Glittering light on water," Opt. Photon. News **10**(3), 43–45, 68 (1999).
33. J. W. Salisbury, A. Basu, and E. M. Fischer, "Thermal infrared spectra of lunar soils," Icarus **130,** 125–139 (1997).
34. F. H. Murcray, D. G. Murcray, and W. J. Williams, "Infrared emissivity of lunar surface features. 1. Balloon-borne observations," J. Geophys. Res. **75,** 2662–2669 (1970).
35. H. K. Kieffer and R. L. Wildey, "Establishing the moon as a spectral radiance standard," J. Atmos. Oceanic Technol. **13,** 360–375 (1996).